magnetochemistry

MDPI

Article

Theory of Antiferromagnet-Based Detector of Terahertz Frequency Signals

Ansar Safin [1,2,*], Sergey Nikitov [1,3], Andrei Kirilyuk [1,4], Vasyl Tyberkevych [5] and Andrei Slavin [5]

[1] Kotel'nikov Institute of Radioengineering and Electronics, Russian Academy of Sciences, 125009 Moscow, Russia; nikitov@cplire.ru (S.N.); andrei.kirilyuk@ru.nl (A.K.)
[2] Department of Radioengineering and Electronics, Moscow Power Engineering Institute, National Research University, 111250 Moscow, Russia
[3] Moscow Institute of Physics and Technology, Dolgoprudny, 141700 Moscow, Russia
[4] FELIX Laboratory, Radboud University, 6525 AJ Nijmegen, The Netherlands
[5] Department of Physics, Oakland University, Rochester, MI 48309, USA; tyberkev@oakland.edu (V.T.); slavin@oakland.edu (A.S.)
* Correspondence: arsafin@gmail.com

Abstract: We present a theory of a detector of terahertz-frequency signals based on an antiferromagnetic (AFM) crystal. The conversion of a THz-frequency electromagnetic signal into the DC voltage is realized using the inverse spin Hall effect in an antiferromagnet/heavy metal bilayer. An additional bias DC magnetic field can be used to tune the antiferromagnetic resonance frequency. We show that if a *uniaxial* AFM is used, the detection of linearly polarized signals is possible only for a non-zero DC magnetic field, while circularly polarized signals can be detected in a zero DC magnetic field. In contrast, a detector based on a *biaxial* AFM can be used without a bias DC magnetic field for the rectification of both linearly and circularly polarized signals. The sensitivity of a proposed AFM detector can be increased by increasing the magnitude of the bias magnetic field, or by by decreasing the thickness of the AFM layer. We believe that the presented results will be useful for the practical development of tunable, sensitive and portable spintronic detectors of THz-frequency signals based of the antiferromagnetic resonance (AFMR).

Keywords: spin pumping; spin-orbit torque; insulating antiferromagnet; sub-terahertz waves; spin-Hall effect

Citation: Safin, A.; Nikitov, S.; Kirilyuk, A.; Tybekevych, V.; Slavin, A. Theory of Antiferromagnet-Based Detector of Terahertz Frequency Signals. *Magnetochemistry* **2022**, *8*, 26. https://doi.org/10.3390/magnetochemistry8020026

Academic Editor: Raymond F. Bishop

Received: 31 December 2021
Accepted: 8 February 2022
Published: 12 February 2022

1. Introduction

Frequency-selective and tunable detection of terahertz (THz) frequency signals is an operation that is important for many different applications—from medical scanning, to security, to high-speed 6G communication and radio astronomy [1]. Due to the rarity of resonators with natural frequencies in the THz (from 0.1 to 10 THz) frequency range, the tunable resonance detection in this frequency range is still a significant challenge [2–5]. One option to realize resonance detection of THz-frequency signals is to use antiferromagnetic (AFM) crystals that naturally have frequencies of the antiferromagnetic resonance (AFMR) in the THz-frequency range. These high frequencies of the AFMR are related to the existence of a strong exchange interaction between the AFM magnetic sublattices (internal exchange magnetic fields of up to 10^2–10^3 T) [6].

It has been shown theoretically that AFMs can be used as active layers of THz-frequency oscillators [7–10] and detectors [11–13]. Recent experiments on the effect of spin-pumping performed in both uniaxial [14–16] and biaxial [17,18] AFMs indicate the possibility of development of THz frequency-detectors based on antiferromagnet/heavy metal (AFM/HM) heterostructures. In this work, we analyze the available theoretical and experimental data on the properties of AFM crystals, and describe the influence of the AFM crystal anisotropy, magnitude and orientation of the external bias magnetic field,

as well as the polarization of the received THz-frequency electromagnetic signal, on the possibility of resonance detection of such signals using spin pumping in passive spintronic detectors-based AFM/HM bilayers.

The general theory of spin-pumping and spin-transfer torque in AFM/HM layered structures was developed in [19]. The influence of the signal polarization and the type of the AFM anisotropy on the detection of THz-frequency signals by the AFM/HM spintronic detectors has been further studied theoretically in [11,13]. It was found that a *uniaxial* AFM gives a zero rectified voltage for a *linearly* polarized AC spin current signal, but can detect a *circularly* polarized AC signal [13]. It was also found that a *biaxial* dielectric AFM (such as NiO) can be used as a sensitive element of a resonance quadratic rectifier of *linearly* polarized AC spin current signals, and that a sensitivity of such a rectifier could be in the range of 1 kV/W [11,13]. The conditions necessary for using *uniaxial* AFMs for the detection of *linearly* polarized signals have not been studied in detail, so far.

It is well-known (see, e.g., [6]) that, in the absence of an external bias magnetic field, the AFMR frequencies in AFM crystals are proportional to the square root of the product of the anisotropy fields and the AFM internal exchange field. The AFM internal exchange magnetic field, which keeps the AFM sublattices anti-parallel to each other, reaches hundreds of Tesla, while the AFM anisotropy field is much smaller (from μT to several T), and , therefore, the tuning of the AFMR frequency is, usually, done by changing the AFM anisotropy fields. The variation of the anisotropy fields can be done using magnetostriction in the adjacent piezoelectric layer [20,21], driving DC current through the adjacent HM layer [13], or by changing temperature [22]. When an external bias magnetic field is applied to a uniaxial AFM, its influence on the AFMR frequency depends on the field direction relative to the anisotropy easy axis, and linear tuning of the AFMR frequency is possible when the bias field is parallel to the anisotropy easy axis, but the bias field magnitude necessary for the AFMR tuning is rather large, of the order of several tesla.

In this work, we consider a theory of resonance detection of both *linearly* and *circularly* polarized electromagnetic (EM) signals via a spin-pumping mechanism in AFM/HM heterostructures. We assume the presence of a DC external bias magnetic field that can be used for tuning the AFMR frequency of the detector, as it was done in recent AFM spin-pumping experiments [14–16]. We also study the additional influence of the bias magnetic field on the detector properties. The paper is organized as follows. In Section 2, we describe the possible physical structure of an AFM/HM based detector. In Section 3, we present a mathematical model of the magnetization dynamics in an AFM using the so-called "sigma-model" developed in [23–25] for both uniaxial and biaxial AFM crystals. The expressions for the AFM-based detector sensitivity are presented in Section 4, while the conclusions are given in Section 5.

2. Physical Structure

Let us consider a concept of a THz-frequency detector based on AFM/HM bilayer, which is shown in Figure 1a. Here, the anisotropy easy-axis is oriented in the plane of the sample $\mathbf{e}_{\mathrm{EA}} = \mathbf{e}_3$. The magnetic field component of the AC electromagnetic field $\mathbf{h}_{AC} = h_{AC}\mathbf{e}_{\mathrm{AC}} \cdot e^{i\omega t}$ created by an external signal is oriented in the plane perpendicular to the easy-axis $\mathbf{e}_{\mathrm{EA}}$, where $\mathbf{e}_{\mathrm{AC}} = (\mathbf{e}_1 + \mathbf{e}_2)/\sqrt{2}$ and $\mathbf{e}_{\mathrm{AC}} = (\mathbf{e}_1 + i\mathbf{e}_2)/\sqrt{2}$ for the cases of linear (LP) and circular (CP) polarization, respectively, while h_{AC} and ω are the amplitude and frequency of the AC magnetic field.

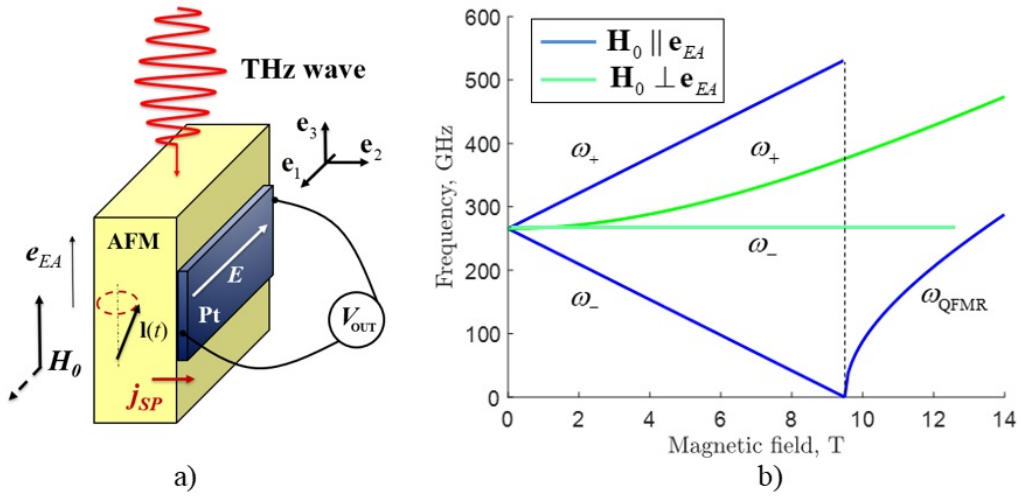

Figure 1. (**a**) Schematic view of the resonance detector based on an AFM/HM heterostructure under the action of a THz-frequency electromagnetic signal with controllable polarization. Here **l**(t) is the Neel vector oriented along the anisotropy easy-axis, V_{OUT} is the output DC electric voltage, and $\mathbf{H_0}$ is the external DC bias magnetic field; (**b**) dependence of the resonance frequencies of the detector based on the uniaxial AFM MnF_2 on the DC bias magnetic field H_0 for $\mathbf{H}_0 \parallel \mathbf{e}_{\mathrm{EA}}$ and $\mathbf{H}_0 \perp \mathbf{e}_{\mathrm{EA}}$.

The external AC magnetic field induces torque, which acts on the magnetic sublattices of the AFM, and causes oscillations of the Néel vector $\mathbf{l} = (\mathbf{M}_1 - \mathbf{M}_2)/2M_s$ near the easy-axis, and creates a spin-current due to the spin-pumping mechanism [6]:

$$\mathbf{j}_{SP} = \frac{\hbar g_r}{2\pi}\left[\mathbf{l} \times \frac{d\mathbf{l}}{dt}\right], \tag{1}$$

where g_r is the real part of the spin-mixing conductance, $\hbar$ is the reduced Planck constant, $\mathbf{M}_{1,2}$ are magnetization vectors of the AFM sublattices, and M_s is the saturation magnetization of the sublattices. This spin current is then injected into the HM, which produces a charge current and electric field between the output electrodes E through the inverse spin Hall effect (ISHE), and results in an electric DC voltage V_{OUT}. The experimental ISHE voltages and other physical parameters of different uniaxial and biaxial AFMs for the zero external DC magnetic field are presented in Table 1, and they are all above tens of nV. One can see from Table 1 the resonance frequencies of the presented AFMs lie in the THz frequency range. We use MnF_2 and NiO for our numerical simulations for uniaxial and biaxial cases, respectively, as materials with low damping at room temperatures, which give the acceptable quality factor for AFM resonance.

Table 1. Parameters of uniaxial and biaxial AFMs at zero DC magnetic field $H_0 = 0$.

Material	$H_{\mathrm{EA,HA}}$, T	H_{ex}, T	f_{AFMR}, GHz	Δf, GHz	V_{ISHE}, nV	Ref.
FeF_2	20	108	1400	30	-	[26,27]
Cr_2O_3	0.07	490	163	5.6	30	[15,17]
MnF_2	0.85	106	245	2.6	60	[14,16]
NiO	0.03, 0.7668	1937	220, 1100	18	-	[28,29]

3. Magnetization Precession Induced by a Polarized THz EM Signal

A general phenomenological method for the description of the AFM dynamics is based on the use of coupled Landau–Lifshitz equations for the magnetizations of the sublattices $\mathbf{M}_{1,2}$ [6]. Using this approach under the condition that the total magnetization $\mathbf{M} = \mathbf{M}_1 + \mathbf{M}_2$ is small, I.V. Baryakhtar and B.A. Ivanov [23] obtained an effectively closed equation describing the dynamics of an antiferromagnet in terms of a normalized (unit)

vector $\mathbf{l} = (\mathbf{M}_1 - \mathbf{M}_2)/2M_s$. In their derivation, it was assumed that the magnetization vector M of an antiferromagnet is a "slave" variable, and is determined by the vector $\mathbf{l}(t)$ and its time derivative $d\mathbf{l}(t)/dt$. The dynamic equations of motion for the unit vector $\mathbf{l}(t)$ are usually called the equations of the "sigma-model", and their application greatly simplifies the analysis of both linear and nonlinear dynamic effects in antiferromagnets [6]. A.F. Andreev and V.I. Marchenko [25], as well as A.K. Zvezdin [24], obtained the sigma-model equation based on the analysis of the dynamic symmetry of the AFM. In this section, we describe the magnetization dynamics in an AFM crystal using the sigma-model in the following form [23,25]:

$$\mathbf{l} \times \left(\frac{d^2\mathbf{l}}{dt^2} + \gamma_{\text{eff}} \frac{d\mathbf{l}}{dt} - 2\gamma \left[\frac{d\mathbf{l}}{dt} \times \mathbf{H}_0 \right] + \frac{\partial W_{\text{AFM}}}{\partial \mathbf{l}} \right) = \left[\mathbf{l} \times \gamma \frac{d\mathbf{h}_{\text{AC}}}{dt} \right] \times \mathbf{l}, \tag{2}$$

where $\gamma_{\text{eff}} = \alpha_{\text{eff}}\omega_{\text{ex}}$ is the spectral linewidth of the AFM resonance at zero bias magnetic field H_0 [13], α_{eff} is the effective damping including Gilbert constant and spin-pumping term [11], $\gamma = 2\pi \cdot 28$ GHz/T is the gyromagnetic ratio. The vector product $d\mathbf{l}/dt \times \mathbf{H}_0$ is the gyroscopic torque [25] and $W_{\text{AFM}}(\mathbf{l}, \mathbf{H}_0)$ is the magnetic energy density in the presence of the DC bias magnetic field, which can be expressed in the form (see for more details [23,25]:

$$W_{\text{AFM}}(\mathbf{l}, \mathbf{H}_0) = -\frac{\omega_{\text{ex}}\omega_{\text{EA}}}{2}(\mathbf{l} \cdot \mathbf{e}_{\text{EA}})^2 + \frac{\omega_{\text{ex}}\omega_{\text{HA}}}{2}(\mathbf{l} \cdot \mathbf{e}_{\text{HA}})^2 + \frac{\gamma^2}{2}(\mathbf{H}_0 \cdot \mathbf{l})^2. \tag{3}$$

Here characteristic frequencies are defined as follows: $\omega_{\text{ex}} = \gamma H_{\text{ex}}$, $\omega_{\text{EA}} = \gamma H_{\text{EA}}$, $\omega_{\text{HA}} = \gamma H_{\text{HA}}$, and H_{ex} is the AFM internal exchange magnetic field, $H_{\text{EA}}, H_{\text{HA}}$ are the AFM anisotropy fields corresponding to the easy and hard axes, respectively (see Table 1). Some authors use a definition of the exchange field in an AFM, $H_{\text{E}} = H_{\text{ex}}/2$, which is half of the exchange field H_{ex} used in our current work. We use the definition $H_{\text{ex}} = 2 \cdot H_{\text{E}}$. following the classical papers on the magnetization dynamics in AFM crystals [23,25]. Thus, the left-hand side part in Equation (2) contains the inertial, damping, gyroscopic, and anisotropy terms, respectively, while the right-hand side part of the equation describes the influence of the AC magnetic field of the external signal. Note, that in [11,13] an AC spin current with a torque $[\mathbf{l} \times \mathbf{j}_{\text{AC}}] \times \mathbf{l}$ in the right-hand side of Equation (2) was used as an excitation mechanism, where $\mathbf{j}_{\text{AC}}$ is the density of the spin-current. Our further results on the study of model (2) with external electromagnetic radiation are also applicable to the case of a spin current.

Let us now consider the small-amplitude dynamics of the Néel vector expressed as a sum of the static component $\mathbf{l}_0$, describing the AFM ground state, and a small dynamic vector $\mathbf{s}(t)$ excited by the AC magnetic field of the external signal:

$$\mathbf{l}(t) = \mathbf{l}_0 + \mathbf{s}(t). \tag{4}$$

Note, that the vectors $\mathbf{l}_0$ and $\mathbf{s}$ satisfy the orthogonality constraint, i.e., $(\mathbf{l}_0 \cdot \mathbf{s}) = 0$. The ansatz (4) uses the assumption of a small change in the dynamic vector $\mathbf{s}(t)$ near the stationary vector $\mathbf{l}_0$, which describes the AFM ground state. This is a common technique in the theory of oscillations and waves. In such a linear theory it is assumed that the vector $\mathbf{s}(t)$ is small, and we can linearize the original nonlinear sigma-model equation to obtain a linear dynamic equation for the vector $\mathbf{s}(t)$. In a nonlinear case, the ansatz $\mathbf{l} = \mathbf{l}_0 + \mathbf{s}$ can also be used, but, then, Equation (6) must be modified, and the nonlinear terms must be considered in that equation. Such nonlinear dynamics can include the second harmonic generation [30], or the appearance of the self-oscillations [8], but the theory of such nonlinear processes is beyond the scope of our current manuscript.

The equation defining the AFM ground state Néel vector $\mathbf{l}_0$ can be easily found from (3) as follows:

$$\omega_{\text{ex}}\omega_{\text{EA}}(\mathbf{l}_0 \cdot \mathbf{e}_{\text{EA}})[\mathbf{l}_0 \times \mathbf{e}_{\text{EA}}] - \omega_{\text{ex}}\omega_{\text{HA}}(\mathbf{l}_0 \cdot \mathbf{e}_{\text{HA}})[\mathbf{l}_0 \times \mathbf{e}_{\text{HA}}] = \omega_{\text{H}}^2(\mathbf{l}_0 \cdot \mathbf{e}_{\text{H}})[\mathbf{l}_0 \times \mathbf{e}_{\text{H}}], \tag{5}$$

where $\omega_{\mathrm{H}} = \gamma H_0$, and $\mathbf{e}_{\mathrm{H}}$ is the unit vector along the DC bias magnetic field. Solving Equation (5) gives the ground state Néel vector $\mathbf{l}_0 = \mathbf{e}_3$.

Using Equation (4) in Equation (2) we can derive the following differential equation describing the oscillations of the dynamic part of the Néel vector $\mathbf{s} = s_1\mathbf{e}_1 + s_2\mathbf{e}_2$:

$$\frac{d^2\mathbf{s}}{dt^2} + \gamma_{\mathrm{eff}}\frac{d\mathbf{s}}{dt} - 2\omega_{\mathrm{H}}(\mathbf{l}_0 \cdot \mathbf{e}_{\mathrm{H}}) \cdot \hat{\Theta} \cdot \frac{d\mathbf{s}}{dt} + \left(\hat{\Omega} - (\mathbf{l}_0 \cdot \hat{\Omega}\mathbf{l}_0)\hat{I}\right) \cdot \mathbf{s} = \hat{\Theta} \cdot \gamma\frac{d\mathbf{h}_{\mathrm{AC}}}{dt}, \tag{6}$$

where matrices $\hat{\Theta}$,$\hat{I}$, $\hat{\Omega}$ can be expressed as follows:

$$\hat{\Theta} = \begin{pmatrix} 0 & 1 \\ -1 & 0 \end{pmatrix}, \hat{I} = \begin{pmatrix} 1 & 0 \\ 0 & 1 \end{pmatrix}, \tag{7}$$

$$\hat{\Omega} = -\omega_{\mathrm{ex}}\omega_{\mathrm{EA}}\mathbf{e}_{\mathrm{EA}} \otimes \mathbf{e}_{\mathrm{EA}} + \omega_{\mathrm{ex}}\omega_{\mathrm{HA}}\mathbf{e}_{\mathrm{HA}} \otimes \mathbf{e}_{\mathrm{HA}} + \omega_{\mathrm{H}}^2\mathbf{e}_{\mathrm{H}} \otimes \mathbf{e}_{\mathrm{H}}. \tag{8}$$

Linear vectorial Equation (6) describes the small-amplitude dynamics of the AFM Néel vector. The formal solution $\mathbf{s}(\omega)$ of Equation (6) for a harmonic driving signal $\mathbf{h}_{\mathrm{AC}} = \omega_{\mathrm{AC}}\mathbf{e}_{\mathrm{AC}}e^{i\omega t}$ (here $\omega_{\mathrm{AC}} = \gamma h_{\mathrm{AC}}$) has the following form:

$$\mathbf{s}(\omega) = i\omega\omega_{\mathrm{AC}}\hat{D}^{-1}(\omega) \cdot \hat{\Theta} \cdot \mathbf{e}_{\mathrm{AC}}, \tag{9}$$

where $\hat{D}(\omega)$ is the matrix

$$\hat{D}(\omega) = \left[\left(-\omega^2 + i\gamma_{\mathrm{eff}}\omega\right)\hat{I} - 2i\omega\omega_{\mathrm{H}}(\mathbf{l}_0 \cdot \mathbf{e}_{\mathrm{H}})\hat{\Theta} + (\hat{\Omega} - (\mathbf{l}_0 \cdot \hat{\Omega}\mathbf{l}_0)\hat{I})\right]. \tag{10}$$

We can rewrite expression (9) in the form:

$$\begin{pmatrix} s_1 \\ s_2 \end{pmatrix} = \frac{i\omega\omega_{\mathrm{AC}}}{\det\left[\hat{D}(\omega)\right]}\begin{pmatrix} \omega_2^2 - \omega^2 + i\omega\gamma_{\mathrm{eff}} & 2i\omega\omega_{\mathrm{H}}(\mathbf{e}_{\mathrm{H}} \cdot \mathbf{l}_0) \\ -2i\omega\omega_{\mathrm{H}}(\mathbf{e}_{\mathrm{H}} \cdot \mathbf{l}_0) & \omega_1^2 - \omega^2 + i\omega\gamma_{\mathrm{eff}} \end{pmatrix} \cdot \begin{pmatrix} e_{\mathrm{AC},2} \\ -e_{\mathrm{AC},1} \end{pmatrix}, \tag{11}$$

where $e_{\mathrm{AC},1,2} = 1/\sqrt{2}$ for LP and $e_{AC,2} = i/\sqrt{2}$, $e_{AC,1} = 1/\sqrt{2}$ for CP, and

$$\omega_{1,2}^2 = \omega_{\mathrm{ex}}(\omega_{\mathrm{EA}} + \omega_{\mathrm{HA}}(\mathbf{e}_{1,2} \cdot \mathbf{e}_{\mathrm{HA}})) + \omega_{\mathrm{H}}^2 \cdot \left((\mathbf{e}_{1,2} \cdot \mathbf{e}_{\mathrm{H}})^2 - (\mathbf{e}_3 \cdot \mathbf{e}_{\mathrm{H}})^2\right). \tag{12}$$

Now, we can find a general expression for the AFM eigenfrequencies $\omega_{\pm}$ in the case of zero effective damping γ_{eff} . These eigenfrequencies are found from the condition of the vanishing of the determinant of the matrix (10) in the following form (here we take $\overline{\omega}_{\mathrm{H}} = \omega_{\mathrm{H}} : (\mathbf{e}_{\mathrm{H}} \cdot \mathbf{l}_0)$):

$$\omega_{\pm}^2 = \frac{1}{2}\left(\omega_1^2 + \omega_2^2\right) + 2 \cdot \overline{\omega}_{\mathrm{H}}^2 \pm \sqrt{\frac{1}{4}\left(\omega_1^2 - \omega_2^2\right)^2 + 2 \cdot \overline{\omega}_{\mathrm{H}}^2\left(\omega_1^2 + \omega_2^2\right) + 4\overline{\omega}_{\mathrm{H}}^4} \tag{13}$$

Let us consider several particular cases for the orientation of the external bias magnetic field $\mathbf{H}_0$ relative to the axes $\mathbf{e}_{1,2,3}$ in the uniaxial and biaxial AFM crystals.

(a) Easy-axis uniaxial AFM ($H_{HA} = 0$).

For the case of a zero DC bias magnetic field, two eigenfrequencies $\omega_{\pm}$ are degenerate, and equal to $\omega_{\pm} = \sqrt{\omega_{\mathrm{ex}}\omega_{\mathrm{EA}}} = \omega_{\mathrm{AFMR}}^0$. The dynamic vector $\mathbf{s}(\omega)$ has, in this case, the simplest form:

$$\begin{pmatrix} s_1 \\ s_2 \end{pmatrix} = \frac{i\omega\omega_{\mathrm{AC}}}{\left(-\omega^2 + (\omega_{\mathrm{AFMR}}^0)^2 + i\omega\gamma_{\mathrm{eff}}\right)} \cdot \begin{pmatrix} e_{\mathrm{AC},2} \\ -e_{\mathrm{AC},1} \end{pmatrix}. \tag{14}$$

This is a standard expression for the amplitude–frequency characteristic of an oscillatory system with one degree of freedom FM modes are (two AFM modes $s_{1,2}$ are degenerate and uncoupled).

In the case when $\mathbf{H}_0 \parallel \mathbf{e}_{\mathrm{EA}}$, the resonance frequencies from (13) can be found in the following form:

$$\omega_{\pm} = \omega^0_{\mathrm{AFMR}} \pm \omega_{\mathrm{H}} \quad \text{for} \quad H_0 < H_{sf}, \tag{15}$$

and

$$\omega_{\mathrm{QFMR}} = \sqrt{(\omega_{\mathrm{H}})^2 - (\omega^0_{\mathrm{AFMR}})^2} \quad \text{for} \quad H_0 > H_{sf}, \tag{16}$$

where $H_{\mathrm{sf}} = \sqrt{H_{\mathrm{ex}} \cdot H_{\mathrm{EA}}}$ is the spin-flop field, at which the Néel vector changes its direction from the parallel to the external bias magnetic field to the perpendicular to it. The dependences of the resonant frequencies defined by the expressions (15) and (16) are shown in Figure 1b. Such dependences were obtained experimentally for different easy-axis AFMs (see, e.g., [15,16]). Since the rectification of the modes having "quasi-ferromagnetic" frequency requires a bias field higher than the field of a spin-flop transition (which for MnF_2 is 9.4 T, and for Cr_2O_3 is 6 T), and, therefore, requires the use of sources of rather large magnetic fields, in the following we shall restrict our attention to the rectification of signals in bias fields below the spin-flop transition.

In the case when $\mathbf{H}_0 \perp \mathbf{e}_{\mathrm{EA}}$, the AFMR frequencies are:

$$\omega_{+} = \sqrt{\left(\omega^0_{\mathrm{AFMR}}\right)^2 + \omega^2_{\mathrm{H}}}, \quad \omega_{-} = \omega^0_{\mathrm{AFMR}}, \tag{17}$$

The upper frequency quadratically increases with the increase of the DC bias magnetic field, while the lower mode frequency is constant and equal to ω^0_{AFMR}.

(b) Easy-plane biaxial AFM ($H_{HA} \neq 0$.)

For the zero DC bias magnetic field two AFM frequencies $\omega_{\pm}$ are non-degenerate and equal to $\sqrt{\omega_{\mathrm{ex}}\omega_{\mathrm{EA}}}$ and $\sqrt{\omega_{\mathrm{ex}}(\omega_{\mathrm{HA}} + \omega_{\mathrm{EA}})}$. Most often, the hard-axis field H_{HA} is much larger than the easy-axis field H_{EA} (see Table 1 for the nickel oxide), and the effect of the easy-plane anisotropy variation on the higher resonance frequency can be neglected. Qualitatively, the nature of the dependences shown in Figure 1b coincides for the easy-axis and the easy-plane cases.

In the particular case when $\mathbf{H}_0 || \mathbf{e}_{\mathrm{EA}}$ and $\mathbf{e}_{\mathrm{HA}} = \mathbf{e}_1$ the resonance frequencies are equal to (before the spin-flop field [29]):

$$\omega_{+} \approx \sqrt{\omega_{\mathrm{ex}}\omega_{\mathrm{HA}} + 3\omega^2_{\mathrm{H}}}, \quad \omega_{-} \approx \sqrt{\omega_{\mathrm{ex}}\omega_{\mathrm{EA}} - \omega^2_{\mathrm{H}}}. \tag{18}$$

For the $\mathbf{H}_0 \perp \mathbf{e}_{\mathrm{EA}}$ one of the AFMR frequencies does not depend on the magnetic field, and the second one grows quadratically.

Let us now study the influence of the driving AC signal polarization on the rectified DC voltage in AFM obtained as a result of the spin pumping for various relative orientations between the direction of the external bias DC magnetic field and the anisotropy axes.

4. Rectification of THz-Frequency Electromagnetic Signals

Let us derive an expression for the inverse spin Hall DC voltage V_{OUT} induced by the spin pumping from the AFM into the adjacent HM layer. Using (1) and (4) we get this expression in the following form:

$$V_{\mathrm{OUT}} = \kappa \langle s_1 \frac{ds_2}{dt} - s_2 \frac{ds_1}{dt} \rangle = 2i\omega\kappa[s_1^* s_2 - s_2^* s_1], \tag{19}$$

where κ is the proportionality coefficient

$$\kappa = \frac{L g_r \theta_{\mathrm{SH}} e \lambda_{\mathrm{Pt}} \rho}{2\pi d_{\mathrm{Pt}}} \tanh\left(\frac{d_{\mathrm{Pt}}}{2\lambda_{\mathrm{Pt}}}\right), \tag{20}$$

L is the distance between output electrodes, θ_{SH} is the spin-Hall angle, e is the electron charge, λ_{Pt} is the spin-diffusion length, while ρ and d_{Pt} are the electrical resistivity

and thickness of the Pt layer, respectively. For the input AC power of the EM signal $P_{AC} = \frac{c}{2\mu_0} S \cdot (h_{\rm AC})^2$, where c is the speed of light, μ_0 is the magnetic permeability, S is the AFM layer cross-section, one can find the detector sensitivity defined as:

$$R(\omega) = \frac{|V_{\rm OUT}(\omega)|}{P_{\rm AC}} \tag{21}$$

For the cases of linear and circular polarizations of the driving AC signal we get the detector sensitivities as:

$$R_{\rm LP}(\omega) = R_0 \cdot \frac{\omega_{\rm ex}\omega^3 |(\omega_1^2 - \omega^2)(\omega\gamma_{\rm eff} + 2\omega\overline{\omega}_{\rm H}) - (\omega_2^2 - \omega^2)(\omega\gamma_{\rm eff} - 2\omega\overline{\omega}_{\rm H})|}{|\det(\hat{D}(\omega))|^2}, \tag{22}$$

$$R_{\rm CP}(\omega) = R_0 \cdot \frac{\omega_{\rm ex}\omega^3 |(\omega_1^2 - \omega^2 - 2\omega\overline{\omega}_{\rm H})(\omega_2^2 - \omega^2 - 2\omega\overline{\omega}_{\rm H}) + (\omega\gamma_{\rm eff})^2|}{|\det(\hat{D}(\omega))|^2}, \tag{23}$$

where $R_0 = 4\kappa\gamma^2\mu_0/(S\omega_{\rm ex}c)$.

Now, let us analyze the above obtained expressions (22) and (23) for detector sensitivity in two different cases of uniaxial and biaxial AFM crystals.

(a) Easy-axis uniaxial AFM ($H_{HA} = 0$).

The rectified output DC voltage is equal to zero due to the fact, that the modes $s_{1,2}$ are uncoupled for the LP in both cases $H_0 = 0$ and $\mathbf{H}_0 \perp \mathbf{e}_{\rm EA}$. When $\mathbf{H}_0 \parallel \mathbf{e}_{\rm EA}$, two modes $s_{1,2}$ are mutually coupled due to the gyroscopic terms in Equation (2), and a non-zero sensitivity can be obtained from (22):

$$R_{\rm LP}(\omega) = \frac{4R_0\omega_{\rm ex}\omega^4|\omega_1^2 - \omega^2|\omega_{\rm H}}{|\det\hat{D}(\omega)|^2}. \tag{24}$$

One can see from the expression (24) that the detector sensitivity is proportional to the bias DC magnetic field $H_0 = 0$. Figure 2a shows the resonance-type dependence of the sensitivity on the frequency ω for the upper branch ω_+ of the resonance curve shown in Figure 1a in the case of a non-zero external DC bias magnetic field. In our numerical calculations, we assumed that the AFM layer is made of MnF_2, and used the following coefficients taken from [16]: $\alpha_{\rm eff} = 0.5 \times 10^{-3}$, $\theta_{\rm SH} = 0.08$, $\lambda_{Pt} = 1.4$ nm, $d_{Pt} = 5$ nm, $\rho = 2.5 \times 10^{-7}$ $\Omega \cdot$ m, $g_r = 2.86 \times 10^{18}$ m^{-2}, $d_{\rm AFM} = 10$ nm, $L = 100$ µm. As can be seen from Figure 2a and Equation (18), the resonance sensitivity increases with the increase of the the bias magnetic field H_0. Note, that the input AC power of the EM signal is defined as $P_{AC} = \frac{c}{2\mu_0} S \cdot (h_{\rm AC})^2$, so for the AC signal amplitude $h_{\rm AC} = 0.1$ mT and the AFM cross-section $S = 100 \times 100$ nm^2 we get the value of $P_{AC} = 12$ nW. The dependence of the detector sensitivity on the bias magnetic field for linearly polarized (LP) and circularly polarized (CP) signals is shown in Figure 2b for the above given parameters and nano-scale sizes of the AFM/HM heterostructure. When the magnitude of the DC magnetic field is varied, the resonance frequency shifts, as it is shown in Figure 1b, while the spectral linewidth of a resonance curve remains unchanged, as it is equal to $\alpha_{\rm eff} \cdot \omega_{\rm ex}$. In the recent experiment [15,16] performed in bulk mm-size AFM samples the observed detector sensitivity was near $10^{-5} - 10^{-6}$ V/W, which is quite small compared to our above presented theoretical estimation made for a nano-sized AFM sample. We believe that the main reason for this huge difference is the relatively large size of the AFM layer used in [15,16]. It has been also theoretically demonstrated recently [11,13] that the sensitivity of an AFM detector can reach several kV/W for detectors using nanometer-thick AFM layers. As follows from expressions (19) and (20), the output voltage of an AFM detector is inversely proportional to the AFM thickness. As it was shown in [11], when the AFM thickness decreases, there is an optimal AFM thickness at which the sensitivity reaches the maximum value. With a further decrease of the AFM thickness, the sensitivity decreases. To correctly calculate the sensitivity at thicknesses of the order of several nanometers, it is

necessary to use the modified sigma model (2), in which the additional spatial derivatives are included. This calculation was presented in [11], and it is not repeated in our current work. Thus, we come to the obvious conclusion that the nano-sized sensitive AFM elements should be used in the future design of the spintronic AFM detectors of THz-frequency EM signals. Another possible way to increase the detector sensitivity is to use several nano-scale detectors mutually coupled through a common HM layer, or to use magnetic tunnel junctions to extract the output voltage [10].

For a circularly polarized EM signal in both cases $\mathbf{H}_0 \parallel \mathbf{e}_{\mathrm{EA}}$ and $\mathbf{H}_0 \perp \mathbf{e}_{\mathrm{EA}}$, one can get a non-zero diode sensitivity described by the equation:

$$R_{\mathrm{CP}}(\omega) = \frac{R_0 \omega_{\mathrm{ex}} \omega^3 |(\omega_1^2 - \omega^2 - 2\omega\overline{\omega}_{\mathrm{H}})^2 + (\omega\gamma_{\mathrm{eff}})^2|}{|\det \hat{D}(\omega)|^2}. \tag{25}$$

The rectification of a THz signal at a zero bias magnetic field was studied earlier in [13], where the driving THz-frequency signal had the form of a spin-polarized current. However, the presence of an external bias DC magnetic field removes the degeneracy of the eigen-frequencies of the system, and increases the magnitude of the rectified voltage. Additionally, the use of a driving signal with circular polarization makes possible the observation of the rectified spin-pumping voltage both in the presence, and in the absence of an external bias magnetic field. In contrast, in the case of a linear polarization of the driving signal, such an observation is realized only for $\mathbf{H}_0 \parallel \mathbf{e}_{\mathrm{A}}$. As can be seen from Figure 2, the sensitivity for CP signals is larger than for the LP signals at the same value of the DC magnetic field. In the CP case, the expression (25) consists of two terms: one is linearly proportional to the DC magnetic field, while the other one is independent of it. In contrast, in the LP case the sensitivity expression (24) contains only one term proportional to the DC magnetic field. The summary for the calculation of eigen-frequencies $\omega_{\pm}$ and sensitivity at different ratios between the orientation of the external magnetic field is presented in Table 2.

Table 2. Expressions for the eigen-frequencies $\omega_{\pm}$ and AFM diode sensitivity R at different orientations of the external bias magnetic field $\mathbf{H}_0$ relative to the easy axis $\mathbf{e}_{\mathrm{EA}}$ of the AFM layer and polarizations (LP or CP) of the external EM signal for the uniaxial AFM crystal. The numbers in parentheses (·) correspond to the equation numbers in the main text of the paper.

Parameter	$\boldsymbol{H_0 = 0}$	$\mathbf{H}_0 \parallel \mathbf{e}_{\mathrm{EA}}$	$\mathbf{H}_0 \perp \mathbf{e}_{\mathrm{EA}}$
$\omega_{\pm}$	$\sqrt{\omega_{\mathrm{ex}}\omega_{\mathrm{EA}}}$	$\sqrt{\omega_{\mathrm{ex}}\omega_{\mathrm{EA}}} \pm \omega_{\mathrm{H}}$	$\sqrt{\omega_{\mathrm{ex}}\omega_{\mathrm{EA}}}$, $\sqrt{\omega_{\mathrm{ex}}\omega_{\mathrm{EA}} + \omega_{\mathrm{H}}^2}$
R_{LP}	0	(24)	0
R_{CP}	(25)	(25)	(25)

(b) Easy-plane biaxial AFM ($H_{HA} \neq 0$).

It was shown previously [11] that a biaxial AFM can be used to rectify a *linearly* polarized AC spin current in the case when the AFM easy plane is oriented *perpendicular* to the plane of the AFM sample. The maximum value of the rectified voltage is achieved when the angle between the direction of the spin-current polarization and the directions of the AFM anisotropy axes is 45 degrees. In this case, it is possible to obtain a non-zero rectified voltage even in a *zero* bias DC magnetic field.

At the same time, from the technological point of view, it is easier to fabricate biaxial AFM crystal in the case when the easy plane coincides with the plane of the sample, or is inclined to the sample plane at a small angle. In this work, we consider only the situation when the AFM easy plane *coincides* with the plane of the AFM sample.

For the determination of sensitivity in the case of a biaxial AFM one needs to use the general expressions (22) and (23). The analysis presented above for the uniaxial non-degenerate case is applicable to the biaxial case as well. The resonance curve for the NiO is shown in Figure 2c, and is characterized by two resonance eigen-frequencies even in

a zero DC magnetic field. The dependence of the diode sensitivity on the bias magnetic field obtained in such a case is shown in Figure 2d. The sensitivity of the lowest-frequency mode in a zero bias magnetic field and at a linear polarization of the external AC signal is much smaller than for the case of a circular polarization (0.1 V/W for LP and 27 V/W for CP), but it is, in general, non-zero. In our numerical calculations we used the physical parameters for the NiO crystal taken from [28]. It is easy to see that in the case of a biaxial AFM (similar to the above discussed case of a uniaxial AFM), the increase of the DC bias magnetic field leads to the increase of the diode sensitivity.

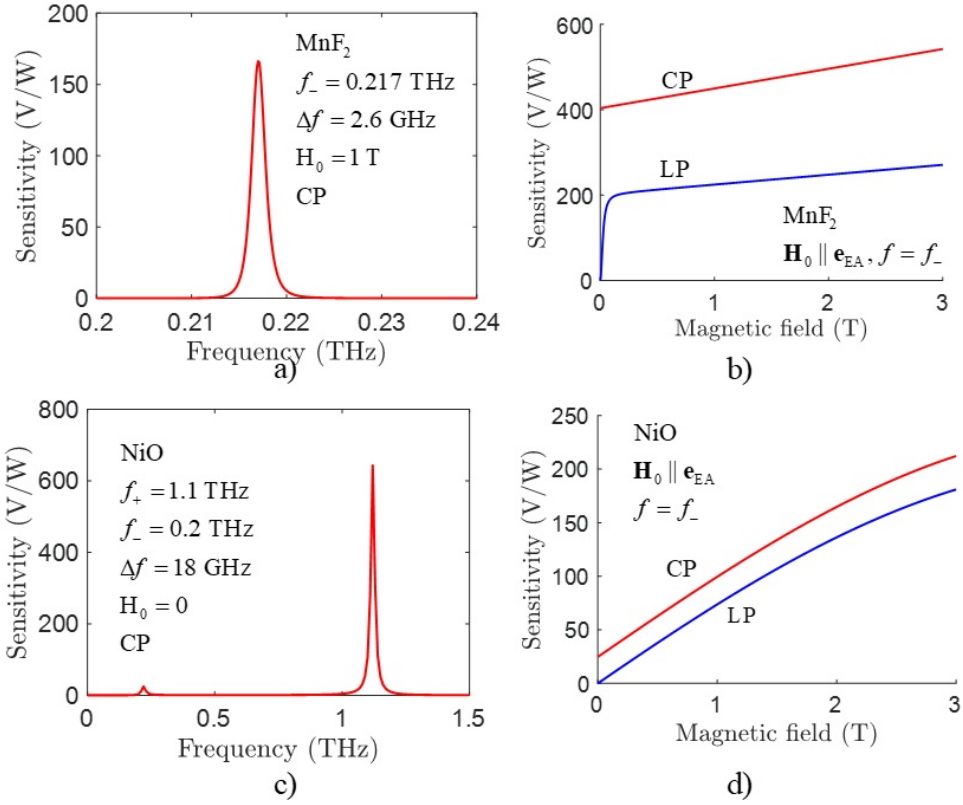

Figure 2. AFM detector sensitivity as a function of the external signal frequency (**a**,**c**) and bias magnetic field (**b**,**d**) for the AFM-HM heterstructures containing uniaxial (MnF_2) and biaxial (NiO) AFM crystals. Calculation were performed for the lowest-frequency AFMR modes).

5. Conclusions

We demonstrated theoretically that nanometer-size AFM/HM heterostructures can be used for the development of sensitive and tunable resonance detectors of THz frequency signals. We found that: (i) Using *uniaxial* AFM crystals the detection of *linearly* polarized electromagnetic signals is possible only for a non-zero DC bias magnetic field, while the signals having *circular* (or elliptical) polarization could be detected even in a zero bias magnetic field; (ii) using *biaxial* AFM crystals it is possible to detect both *linearly* and *circularly* polarized EM signals in a zero bias magnetic field, but in the presence of a bias magnetic field field the detector sensitivity increases with the increase of the bias field for both uniaxial and biaxial AFM crystals; (iii) to increase the sensitivity of an AFM detector it is necessary to decrease the thickness of the sensitive AFM element, since the detection mechanism is based on the interface spin-Hall effect. We believe that our results will be useful for the development of tunable and highly sensitive THz-frequency AFM devices controlled by an applied bias DC magnetic field, such as spectrum analyzers [31] or/and neuromorphic signal processors [28,32].

Author Contributions: Conceptualization, A.S. (Ansar Safin), S.N., A.K., V.T., and A.S. (Andrei Slavin); mathematical model, A. Sa. and V. T., data curation, A.Sa; formal analysis, A.S. (Ansar Safin), A.S and V.T.; writing original draft preparation, A.S. (Ansar Safin); writing review and editing, A.S. (Ansar Safin), S.N., A.K., V.T., and A.S. (Andrei Slavin). All authors have read and agreed to the published version of the manuscript.

Funding: This work was partially funded by the Russian Science Foundation (Grant No. 21-79-10396), U.S. National Science Foundation (Grant # EFMA-1641989), the Air Force Office of Scientific Research under the MURI grant # FA9550-19-1-0307, from the DARPA TWEED grant # DARPA-PA-19-04-05-FP-001, and from the Oakland University Foundation.

Institutional Review Board Statement: Not applicable.

Informed Consent Statement: Not applicable.

Data Availability Statement: The study did not report any data.

Conflicts of Interest: The authors declare no conflict of interests. The funders had no role in the design of the study; in the collection, analysis, or interpretation of data; in the writing of the manuscript, or in the decision to publish the results.

References

1. Dhillon, S.S.; Vitiello, M.S.; Linfield, E.H.; Davies, A.G.; Hoffmann, M.C.; Booske, J.; Paoloni, C.; Gensch, M.; Weightman, P.; Williams, G.P.; et al. The 2017 terahertz science and technology roadmap. *J. Phys. Appl. Phys.* **2017**, *50*, 043001. https://doi.org/10.1088/1361-6463/50/4/043001.
2. Jiang, S.L.; Jia, X.Q.; Jin, B.B.; Kang, L.; Xu, W.W.; Chen, J.; Wu, P.H. Superconducting detectors for terahertz imaging. In Proceedings of the 2015 40th International Conference on Infrared, Millimeter, and Terahertz waves (IRMMW-THz), Hong Kong, China, 23–28 August 2015. https://doi.org/10.1109/irmmw-thz.2015.7327514.
3. Spirito, D.; Coquillat, D.; Bonis, S.L.D.; Lombardo, A.; Bruna, M.; Ferrari, A.C.; Pellegrini, V.; Tredicucci, A.; Knap, W.; Vitiello, M.S. High performance bilayer-graphene terahertz detectors. *Appl. Phys. Lett.* **2014**, *104*, 061111. https://doi.org/10.1063/1.4864082.
4. Viti, L.; Cadore, A.R.; Yang, X.; Vorobiev, A.; Muench, J.E.; Watanabe, K.; Taniguchi, T.; Stake, J.; Ferrari, A.C.; Vitiello, M.S. Thermoelectric graphene photodetectors with sub-nanosecond response times at terahertz frequencies. *Nanophotonics* **2020**, *10*, 89–98. https://doi.org/10.1515/nanoph-2020-0255.
5. Sanchez-Martin, H.; Sanchez-Martin, S.; de-la Torre, I.I.; Perez, S.; Novoa, J.A.; Ducournau, G.; Grimbert, B.; Gaquiere, C.; Gonzalez, T.; Mateos, J. GaN nanodiode arrays with improved design for zero-bias sub-THz detection. *Semicond. Sci. Technol.* **2018**, *33*, 095016. https://doi.org/10.1088/1361-6641/aad766.
6. Baltz, V.; Manchon, A.; Tsoi, M.; Moriyama, T.; Ono, T.; Tserkovnyak, Y. Antiferromagnetic spintronics. *Rev. Mod. Phys.* **2018**, *90*, 015005. https://doi.org/10.1103/revmodphys.90.015005.
7. Cheng, R.; Xiao, D.; Brataas, A. Terahertz Antiferromagnetic Spin Hall Nano-Oscillator. *Phys. Rev. Lett.* **2016**, *116*, 207603. https://doi.org/10.1103/physrevlett.116.207603.
8. Khymyn, R.; Lisenkov, I.; Tiberkevich, V.; Ivanov, B.A.; Slavin, A. Antiferromagnetic THz-frequency Josephson-like Oscillator Driven by Spin Current. *Sci. Rep.* **2017**, *7*, 43705. https://doi.org/10.1038/srep43705.
9. Sulymenko, O.; Prokopenko, O.; Tiberkevich, V.; Slavin, A.; Ivanov, B.; Khymyn, R. Terahertz-Frequency Spin Hall Auto-oscillator Based on a Canted Antiferromagnet. *Phys. Rev. Appl.* **2017**, *8*, 064007. https://doi.org/10.1103/physrevapplied.8.064007.
10. Sulymenko, O.R.; Prokopenko, O.V.; Tyberkevych, V.S.; Slavin, A.N. Terahertz-Frequency Signal Source Based on an Antiferromagnetic Tunnel Junction. *IEEE Magn. Lett.* **2018**, *9*, 1–5. https://doi.org/10.1109/lmag.2018.2852291.
11. Khymyn, R.; Tiberkevich, V.; Slavin, A. Antiferromagnetic spin current rectifier. *AIP Adv.* **2017**, *7*, 055931. https://doi.org/10.1063/1.4977974.
12. Gomonay, O.; Jungwirth, T.; Sinova, J. Narrow-band tunable terahertz detector in antiferromagnets via staggered-field and antidamping torques. *Phys. Rev. B* **2018**, *98*, 104430. https://doi.org/10.1103/physrevb.98.104430.
13. Safin, A.; Puliafito, V.; Carpentieri, M.; Finocchio, G.; Nikitov, S.; Stremoukhov, P.; Kirilyuk, A.; Tyberkevych, V.; Slavin, A. Electrically tunable detector of THz-frequency signals based on an antiferromagnet. *Appl. Phys. Lett.* **2020**, *117*, 222411. https://doi.org/10.1063/5.0031053.
14. Ross, P.; Schreier, M.; Lotze, J.; Huebl, H.; Gross, R.; Goennenwein, S.T.B. Antiferromagentic resonance detected by direct current voltages in MnF_2/Pt bilayers. *J. Appl. Phys.* **2015**, *118*, 233907. https://doi.org/10.1063/1.4937913.
15. Li, J.; Wilson, C.B.; Cheng, R.; Lohmann, M.; Kavand, M.; Yuan, W.; Aldosary, M.; Agladze, N.; Wei, P.; Sherwin, M.S.; et al. Spin current from sub-terahertz-generated antiferromagnetic magnons. *Nature* **2020**, *578*, 70–74. https://doi.org/10.1038/s41586-020-1950-4.
16. Vaidya, P.; Morley, S.A.; van Tol, J.; Liu, Y.; Cheng, R.; Brataas, A.; Lederman, D.; del Barco, E. Subterahertz spin pumping from an insulating antiferromagnet. *Science* **2020**, *368*, 160–165. https://doi.org/10.1126/science.aaz4247.

17. Boventer, I.; Simensen, H.; Anane, A.; Kläui, M.; Brataas, A.; Lebrun, R. Room-Temperature Antiferromagnetic Resonance and Inverse Spin-Hall Voltage in Canted Antiferromagnets. *Phys. Rev. Lett.* **2021**, *126*, 187201.
18. Lebrun, R.; Ross, A.; Gomonay, O.; Baltz, V.; Ebels, U.; Barra, A.L.; Qaiumzadeh, A.; Brataas, A.; Sinova, J.; Kl"aui, M. Long-distance spin-transport across the Morin phase transition up to room temperature in ultra-low damping single crystals of the antiferromagnet α-Fe_2O_3. *Nat. Commun.* **2020**, *11*, 6332. https://doi.org/10.1038/s41467-020-20155-7.
19. Cheng, R.; Xiao, J.; Niu, Q.; Brataas, A. Spin Pumping and Spin-Transfer Torques in Antiferromagnets. *Phys. Rev. Lett.* **2014**, *113*, 057601. https://doi.org/10.1103/physrevlett.113.057601.
20. Popov, P.; Safin, A.; Kirilyuk, A.; Nikitov, S.; Lisenkov, I.; Tyberkevich, V.; Slavin, A. Voltage-Controlled Anisotropy and Current-Induced Magnetization Dynamics in Antiferromagnetic-Piezoelectric Layered Heterostructures. *Phys. Rev. Appl.* **2020**, *13*, 044080. https://doi.org/10.1103/physrevapplied.13.044080.
21. Consolo, G.; Valenti, G.; Safin, A.R.; Nikitov, S.A.; Tyberkevich, V.; Slavin, A. Theory of the electric field controlled antiferromagnetic spin Hall oscillator and detector. *Phys. Rev. B* **2021**, *103*, 134431. https://doi.org/10.1103/physrevb.103.134431.
22. Meshcheryakov, A.A.; Safin, A.R.; Kalyabin, D.V.; Nikitov, S.A.; Mednikov, A.M.; Frolov, D.A.; Kirilyuk, A.I. Temperature tunable oscillator of THz-frequency signals based on the orthoferrite/heavy metal heterostructure. *J. Phys. Appl. Phys.* **2021**, *54*, 195001. https://doi.org/10.1088/1361-6463/abe441.
23. Baryakhtar, I.V.; Ivanov, B.A. About nonlinear waves of magnetization of antiferromagnet. *Sov. J. Low Temp. Phys.* **1979**, *5*, 759–770.
24. Zvezdin, A.K. Dynamics of domain walls in weak ferromagnets. *Pis'ma Zh. Exp. Teor. Fiz.* **1979**, *29*, 605–610.
25. Andreev, A.F.; Marchenko, V.I. Symmetry and the macroscopic dynamics of magnetic materials. *Sov. Phys. Uspekhi* **1980**, *23*, 21–34. https://doi.org/10.1070/pu1980v023n01abeh004859.
26. Ohlmann, R.C.; Tinkham, M. Antiferromagnetic Resonance in FeF_2 at Far-Infrared Frequencies. *Phys. Rev.* **1961**, *123*, 425–434. https://doi.org/10.1103/physrev.123.425.
27. Hutchings, M.T.; Rainford, B.D.; Guggenheim, H.J. Spin waves in antiferromagnetic FeF_2. *J. Phys. Solid State Phys.* **1970**, *3*, 307–322. https://doi.org/10.1088/0022-3719/3/2/013.
28. Khymyn, R.; Lisenkov, I.; Voorheis, J.; Sulymenko, O.; Prokopenko, O.; Tiberkevich, V.; Akerman, J.; Slavin, A. Ultra-fast artificial neuron: Generation of picosecond-duration spikes in a current-driven antiferromagnetic auto-oscillator. *Sci. Rep.* **2018**, *8*, 15727. https://doi.org/10.1038/s41598-018-33697-0.
29. Machado, F.L.A.; Ribeiro, P.R.T.; Holanda, J.; Rodríguez-Suárez, R.L.; Azevedo, A.; Rezende, S.M. Spin-flop transition in the easy-plane antiferromagnet nickel oxide. *Phys. Rev. B* **2017**, *95*, 104418. https://doi.org/10.1103/physrevb.95.104418.
30. Baierl, S.; Mentink, J.; Hohenleutner, M.; Braun, L.; Do, T.M.; Lange, C.; Sell, A.; Fiebig, M.; Woltersdorf, G.; Kampfrath, T.; et al. Terahertz-Driven Nonlinear Spin Response of Antiferromagnetic Nickel Oxide. *Phys. Rev. Lett.* **2016**, *117*, 197201. https://doi.org/10.1103/physrevlett.117.197201.
31. Artemchuk, P.Y.; Sulymenko, O.R.; Louis, S.; Li, J.; Khymyn, R.S.; Bankowski, E.; Meitzler, T.; Tyberkevych, V.S.; Slavin, A.N.; et al. Terahertz frequency spectrum analysis with a nanoscale antiferromagnetic tunnel junction. *J. Appl. Phys.* **2020**, *127*, 063905. https://doi.org/10.1063/1.5140552.
32. Sulymenko, O.; Prokopenko, O.; Lisenkov, I.; Åkerman, J.; Tyberkevych, V.; Slavin, A.N.; Khymyn, R. Ultra-fast logic devices using artificial "neurons" based on antiferromagnetic pulse generators. *J. Appl. Phys.* **2018**, *124*, 152115. https://doi.org/10.1063/1.5042348.